

Localized seismic anisotropy associated with long-term slow-slip events beneath southern Mexico

Teh-Ru Alex Song¹ and YoungHee Kim²

Received 13 February 2012; revised 12 March 2012; accepted 18 March 2012; published 9 May 2012.

[1] Slow slip events (SSEs) are recently discovered in the transition zone downdip of the locked zone where megathrust earthquakes repeatedly occur at subduction zone interface. Structural changes from the locked zone to the transition zone and the nature of in situ deformation in the transition zone, however, remain unclear. We model teleseismic converted P-to-S waves to investigate seismic structural transition and anisotropy associated with shear deformation near the deep locked zone and the transition zone beneath southern Mexico. The deep locked zone appears to be consistent with normal oceanic crust velocity. In the transition zone, we find that seismic anisotropy larger than 5% is associated with the ultra-slow velocity layer (USL) near the top of the subducted oceanic crust. The foliation plane is plunging 20 ± 10 degrees steeper than the plate interface, and it is consistent with crystallographic preferred orientation developed in S-C mylonites. We suggest that long-term SSEs likely coincide with a near-lithostatic semiductile talc-rich shear zone. **Citation:** Song, T.-R. A., and Y. Kim (2012), Localized seismic anisotropy associated with long-term slow-slip events beneath southern Mexico, *Geophys. Res. Lett.*, 39, L09308, doi:10.1029/2012GL051324.

1. Introduction

[2] Episodic slow-slip events (SSEs) were discovered in a number of subduction zones [Beroza and Ide, 2011] where plates move toward each other at a speed several orders of magnitude slower than typical earthquake slip velocity over extended periods of days to years. This relatively unusual slip behaviour is spatially and temporally coupled with semi-continuous high frequency seismic outbursts, or non-volcanic tremors (NVTs). In southern Mexico, the SSEs have long durations (~ 1 year) and they are categorized as long-term SSEs [Kostoglodov et al., 2010; Vergnolle et al., 2010; Radiguet et al., 2011] and are distinct from short-term SSEs [Obara, 2009]. The NVTs are spatially separated from the SSEs while the activities of NVTs can continue without detectable SSEs [Kostoglodov et al., 2010].

[3] The locations of these long-term SSEs have been previously linked to seismic observations such as zones of anomalously ultra-slow velocity layer (USL) [Perez-Campos et al., 2008; Song et al., 2009; Kim et al., 2010] and high Vp/Vs ratio [Kim et al., 2010]. However, it is unclear what is the fundamental property near the plate interface that

gives rise to spatial correlation between SSEs and above mentioned seismic observations and ultimately provides a condition such as very low effective stress that is ideal for the generation of SSEs [Liu and Rice, 2009]. Therefore, it is essential to explore how structural variations near the plate interface can be linked to the style of deformation.

[4] A novel way to elucidate the style of in situ deformation associated with SSEs is to examine seismic velocity anisotropy, where seismic wave speed changes with the direction of incident waves due to deformation induced preferred orientation of minerals [Rey et al., 1994; Fujimoto et al., 2010; Bezacier et al., 2010]. By analyzing azimuthal variations in the polarity and amplitude of teleseismic converted P-to-S waves (or P wave receiver functions) [Frederiksen and Bostock, 2000; Schulte-Pelkum et al., 2005], it is possible to detect fine anisotropic structures on the order of a few kilometres. The orientation for which waves travel fastest (or slowest) can provide a strong evidence on the sense of shearing at the plate interface and indicate the style of deformation (e.g., brittle or ductile, pure shear or simple shear).

2. Observations

[5] We examine P-wave receiver functions recorded by the Middle-America Seismic Experiment (MASE) in southern Mexico that sample the deeper part of the locked zone and the transition zone (Figure 1). Radial component and transverse component seismograms filtered at 0.01–1 Hz are deconvolved with vertical component seismograms at each station using time-domain iterative deconvolution method [Ligorria and Ammon, 1999] and applying a Gaussian filter parameter of 4 to obtain radial and transverse receiver functions, respectively. We stack receiver functions at each station according to earthquake back azimuth and epicentral distance to form linear-interpolated images for southeast, northwest and southwest swathes, respectively (Figure S1 in the auxiliary material).¹ Despite the back azimuth coverage being not great, the observations from these three distinct back azimuths do provide good constraints on the orientation of the symmetry axis and the strength of anisotropy and rule out a large model space. Since we focus on modelling the amplitude of potential converted arrivals relative to the vertical P wave [Cassidy, 1992], the range of back azimuth and epicentral distance is limited within 10 degrees in the stacking procedure, which includes 90% of the entire dataset and contains 3–8 quality traces in different back azimuth bins and stations (see also Figure S1). This procedure minimizes waveform interferences caused by the timing and amplitude variations due to the slab dip and slowness [Cassidy, 1992],

¹Interior for Research on Earth Evolution, Japan Agency for Marine-Earth Science and Technology Center, Yokohama, Japan.

²Lamont-Doherty Earth Observatory, Earth Institute at Columbia University, Palisades, New York, USA.

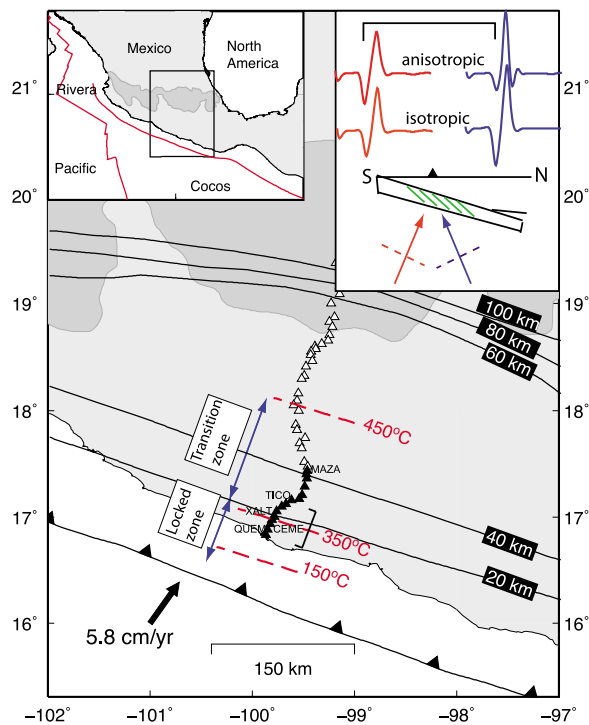


Figure 1. Tectonic map of southern Mexico. Seismic stations from the MASE are shown as triangles. Solid triangles indicate stations included in the stacked receiver function images (Figure S1), which display structural changes across the deep locked zone and the transition zone (see also Figure 2). Red dashed lines show slab surface temperature [Currie *et al.*, 2002]. The upper-right inset illustrates slab geometry and the receiver function expected from an isotropic layer and anisotropic layer. For an isotropic dipping layer, the first negative arrival coming from the north (blue trace) is larger than that coming from the south (red trace). However, for an anisotropic dipping layer with a dipping foliation (green lines), the negative arrival coming from the south is substantially stronger than that coming from the north. Regional plate configurations are shown in the upper-left inset. Black contours represent the isodepth contour of the subducted Cocos slab [Kim *et al.*, 2010].

which varies less than 0.005 s/km within each back azimuth bin.

[6] In general, we can identify a pair of converted arrivals in the radial and transverse receiver functions, sometimes with opposite polarities. These arrivals display a clear image of the subducted Cocos plate dipping inland at a shallow angle of about 18 degrees (Figure S1). Since transverse receiver functions are less consistent than radial receiver functions, we will use azimuthal amplitude pattern recorded in the radial receiver functions to eliminate model parameters that are inconsistent with observations. Subsequently, model parameters are subject to constraints by transverse receiver functions in the northwest back azimuth because more quality traces are used in the stacks and the signal is consistent throughout the dataset. Previously, we used local converted arrivals and receiver functions to reveal strong seismic anisotropy in the topmost 2–6 km of the subducted oceanic mantle [Song and Kim, 2012]. In this study, we

emphasize modeling and discussions on teleseismic converted arrivals that are only relevant to the upper oceanic crust (Figure 2) and the occurrence of SSEs.

[7] Two important observations can be identified. First, the negative converted arrival is anomalously strong in the radial receiver functions (Figures 2 and S2), which can be reconciled with a 3–5 km ultra-slow velocity layer (USL) defined previously by modelling local converted waves [Song *et al.*, 2009], teleseismic underside reflections [Song *et al.*, 2009] and receiver functions [Kim *et al.*, 2010]. However, the amplitude of the first converted arrival in the radial receiver functions abruptly decreases by at least a factor of 2–3 at stations QUEM and CEME closest to the Pacific coast (Figures 2 and S2), suggesting a much smaller S wave velocity contrast between the subducted oceanic crust and the overlying continental crust in the deep locked zone.

[8] Secondly, the amplitudes of the converted arrivals observed in the radial receiver functions in the southeast back azimuth are much larger than those observed in the northwest back azimuth (Figures 2 and S2), especially at station XALT and other stations toward the north sampling the dipping section of the transition zone (Figure 1). We expect exactly the opposite if the USL is an isotropic dipping layer (Figure 1, upper-right inset), indicating that the USL is probably anisotropic. On the other hand, the amplitudes of the converted arrivals observed in the transverse receiver functions in the northwest back azimuth appear very small, typically less than 3% of the P wave amplitude (Figure S1).

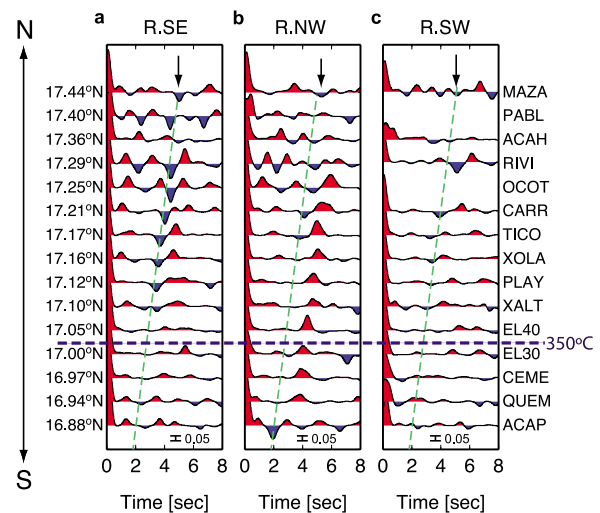


Figure 2. Stacked receiver functions sampling the deep locked zone and the transition zone. Radial receiver functions from (a) back azimuth of southeast (SE), (b) northwest (NW) and (c) southwest (SW). Converted arrivals from the subducted oceanic crust are marked by the solid arrow and green dashed line. The amplitude of the converted arrivals abruptly increases toward the north, crossing the slab surface temperature of about 350°C projected at surface (blue dashed line). The negative converted arrival recorded in the SE swath is much stronger than that recorded in the NW, which is opposite to predictions from isotropic USL (see also Figures 1 and 3a).

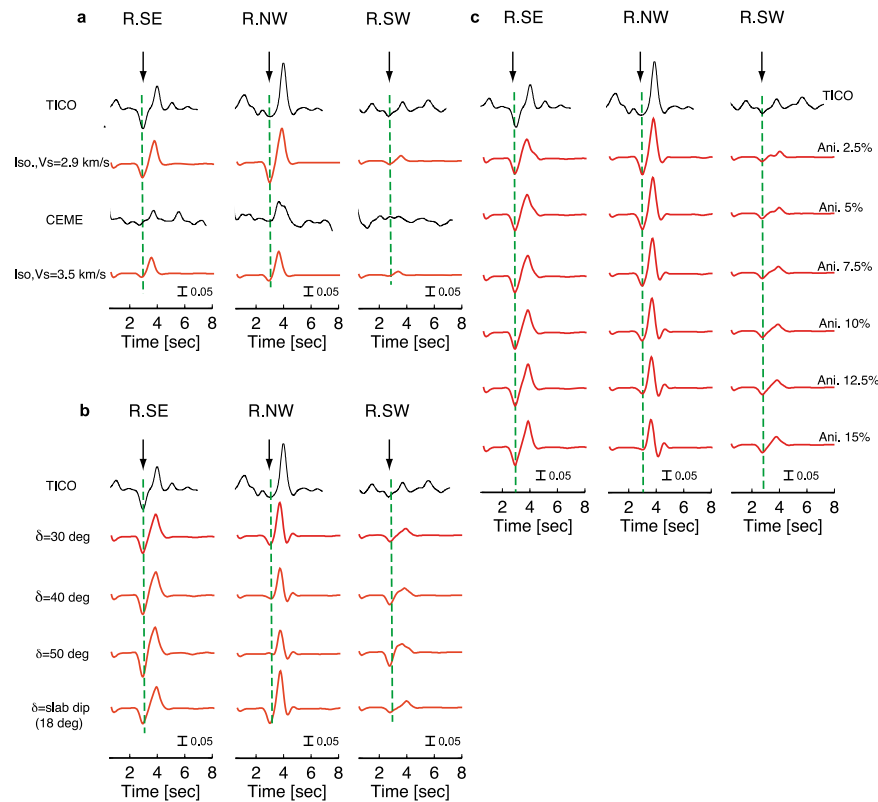


Figure 3. Comparisons of observed and synthetic receiver functions. We examine the sensitivity of observations against (a) isotropic velocity of the upper oceanic crust, (b) the plunge of the fast symmetric axis (FSA) of the anisotropic USL, and (c) the strength of anisotropy of the USL. As shown in Figure 3a, the amplitudes of the converted arrivals at TICO and CEME are dictated by the S wave velocity in the upper oceanic crust. However, azimuthal variations in the amplitudes of the converted arrivals (indicated by solid arrows) at TICO are inconsistent with an isotropic USL model. Instead, the observation is indicative of anisotropic USL and is sensitive to the plunge of the FSA as well as the strength of anisotropy, shown in Figures 3b and 3c. The P-wave and S-wave anisotropy are set at 10% in b and the plunge of FSA is set at 30 degree in Figure 3c. The amplitude scale is indicated as vertical bar.

Those observed in the southeast and southwest back azimuth appear more variable (Figure S1).

3. Receiver Function Modeling

[9] The modeled S wave velocity contrast in the updip section is less than 10%, which is much less than the 25% velocity contrast in the downdip section where the SSEs occur (Figures 2 and 3a) [Song *et al.*, 2009]. With an a priori constraint of slab dip at about 18 degrees [Kim *et al.*, 2010], we compute synthetic receiver functions [Frederiksen and Bostock, 2000] according to the average slowness of the stacked receiver functions in different back azimuth bins (0.062–0.063 s/km in the SE, 0.0502–0.0504 km/s in the NW and 0.041–0.047 s/km in the SW). A grid search is performed to explain the amplitudes of observed converted arrivals in different back azimuths and look for the orientation of the fast symmetric axis (FSA) within the dipping USL and the strength of seismic anisotropy, assuming a hexagonal symmetry (Figures S3 and 4). We also examine an alternative parameterization where the USL anisotropy is modelled by hexagonal symmetry with a slow symmetry axis (SSA) (Figure S3). In the grid search procedure, the isotropic velocity of the USL is allowed to vary by about 10% and the anisotropic parameter η can range from 0.4 to

1.1 (Table S1). As discussed earlier, the model parameters are subject to constraints by the amplitudes of transverse receiver functions in the northwest back azimuth (within $\pm 3\%$ of the P wave amplitude). Since the number of events used in stacking receiver functions is not great (Figure S2), we only provide estimates of anisotropy parameters for the entire dataset within two standard deviations (Figures 4a, 4b, S4, and S5).

[10] We find a peak-to-peak P-wave and S-wave anisotropy of about $10 \pm 5\%$ with the FSA trending at 0 ± 15 degrees north, sub-parallel to the current plate motion direction and plunging 20 ± 10 degrees steeper than the plate interface (slab dip $\sim 20\%$) (Figures 4a and S4). When the USL is parameterized with a SSA, we find that the orientation of the SSA is preferentially oriented toward the south plunging at an angle about 30 to 50 degrees, approximately normal to the preferred orientation of the FSA (Figures 4b and S5). These models predict amplitudes of about 2–10% of the P wave in the transverse receiver functions at the southeast swath, consistent with most of the observations as well (Figure S1). Although our modelling result focuses on reproducing the gross feature across multiple stations, the amplitude of converted arrivals in the northwest swath appears getting stronger at stations north of TICO (Figure 2b) and it could be consistent with an increase (decrease) in the plunge of the

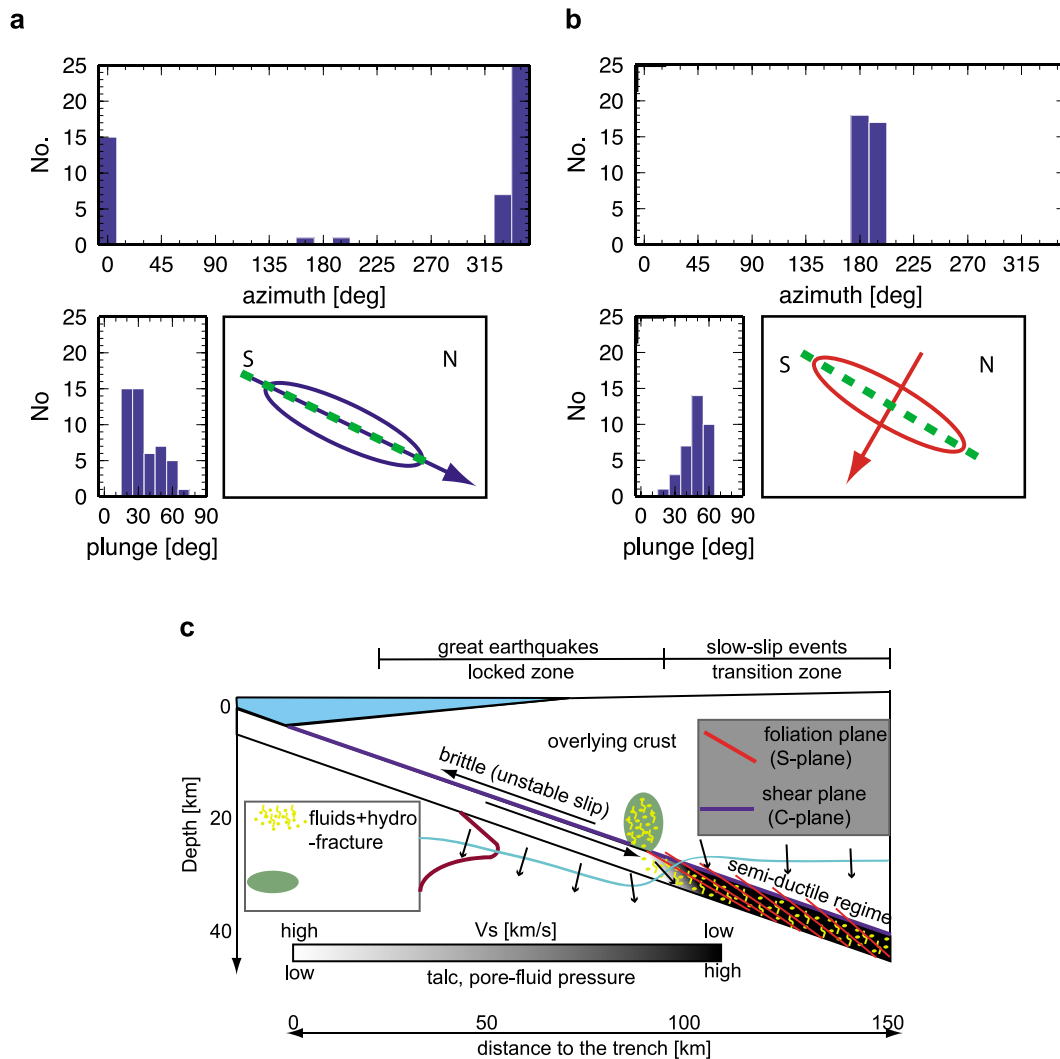


Figure 4. The orientation of inferred foliation from modelling of receiver functions. (a and b) The azimuth and plunge of FSA and SSA, respectively. (c) Schematic diagram of shear zone structure near the plate interface beneath southern Mexico. Great earthquakes primarily occur in the locked zone and a brittle regime with hydrostatic fluid pressure. Slow-slip events (SSEs) predominantly occur in the transition zone and a semiductile regime with a near-lithostatic fluid pressure and very low S wave velocity and strong anisotropy. The rheological transition, marked by the rock pressure profile along the 350°C temperature isocontour (light blue line), exerts an inverted stress gradient (short arrows) that competes with buoyancy force of the fluid and facilitates the formation of the stagnant USL. The fluid in the USL could facilitate hydrofractures, which may episodically breach through the rheological transition into the overlying crust, as evident by minor NVTs activities in a zone of high electric conductivity (see Text S1 in the auxiliary material). We envision that SSEs probably occur within the semi-ductile regime at/near the plate interface.

FSA (SSA) (Figure 3b) or/and a decrease in the strength of anisotropy (Figure 3c).

[11] There exists some trade-offs between the trend and the plunge of the FSA and the strength of anisotropy (Figures 3b and 3c). The isotropic velocity of the USL and anisotropic parameter η could also change the estimate at the trend of the FSA (SSA). However, we can draw a very general conclusion that the anisotropy in the USL has a well-defined plane of symmetry (Figures 4a, 4b, S4, and S5). The acute angle difference between the plane of symmetry and the plate interface is required to explain the azimuthal amplitude variations observed in the receiver functions. While models parameterized with the FSA do explain the data and share the same plane of symmetry determined by

models parameterized with the SSA, the η parameter consistent with the data is generally above 0.9, which is typically the value for upper mantle minerals. We will subsequently focus our discussion on the models parameterized with the SSA.

4. Discussion and Conclusions

[12] The rapid updip decrease in the S wave velocity contrast by about 15–20% is difficult to explain by velocity difference predicted for plausible subducted oceanic crust lithology such as lawsonite blueschist and epidote blueschist, typically less than 7% [Hacker *et al.*, 2003]. While the USL is previously inferred as a high pore fluid pressure layer

because of its low velocity [Song *et al.*, 2009] and high Vp/Vs ratio [Kim *et al.*, 2010], the up dip increase in the S wave velocity may be related to a drop in pore fluid pressure, or a transition from near-lithostatic to hydrostatic regime. In this scenario, the transition in the inferred pore-fluid pressure not only coincides with the lower boundary of earthquake slip zone [Pacheco and Singh, 2010] and slab surface temperature of about 350°C [Currie *et al.*, 2002], but it also coincides with a local zone of high electrical conductivity in the overlying crust [Jödicke *et al.*, 2006].

[13] The localized seismic anisotropy associated with the USL provides a unique and direct access to the in situ rheology. The anisotropic USL may be linked to stress-induced alignment of microcracks along the direction of maximum principal stress [Crampin, 1999], strain-induced crystallographic preferred orientation (CPO) [Rey *et al.*, 1994; Fujimoto *et al.*, 2010; Bezacier *et al.*, 2010] or/and shape-preferred orientation (SPO) by development of fabrics and reorienting different minerals along the foliations [Kern *et al.*, 2008]. For a weak fault, the stress-induced alignment of microcracks is expected to produce anisotropy with the plane of symmetry oriented at a high angle normal to the plate interface, in parallel to the orientation of the maximum principal stress. Considering a crack density of 0.02–0.03 in the USL [Song *et al.*, 2009], the strength of anisotropy caused by the alignment of microcracks is only about 2–3% [Crampin, 1999]. Neither the orientation of the plane of symmetry nor the strength of anisotropy supports the alignment of microcracks as the primary cause for the anisotropic USL.

[14] More likely, the observed seismic anisotropy is predominantly caused by the CPO as well as SPO in the naturally deformed shear zone that is rich in clay minerals [Rey *et al.*, 1994; Godfrey *et al.*, 2000]. The orientation of the plane of symmetry and the relatively low anisotropic parameter η ($\sim 0.7 \pm 0.1$) populated in our grid search modelling (Figure S5) are consistent with laboratory measurement of anisotropy symmetry of deformed phyllosilicates [Godfrey *et al.*, 2000]. We suggest that talc, one of the most abundant clay minerals in subduction zones [Hacker *et al.*, 2003; Mainprice *et al.*, 2008], could be pervasive in the transition zone where SSEs occur. However, a shallow-dipping talc-rich layer by itself does not produce high Vp/Vs ratio constrained by receiver functions [Kim *et al.*, 2010], suggesting the coexistence of high pore fluid pressures in the deformed shear zone near the plate interface.

[15] Our observation strongly indicates that homogeneous deformation takes place over kilometre-scale thickness in a predominantly ductile regime near plate interface (Figure 4c). Typically, cataclastic deformation takes place in the brittle regime with random fabrics and little anisotropy is expected associated with either CPO or SPO. Instead, the acute angle between the plane of symmetry of the anisotropic USL and the plate interface closely mimics the geometric relationship between the S surface (foliation plane) and C surface (shear plane) commonly defined in S-C mylonites [Berthe, 1979; Ramsay, 1980; Lister and Snoke, 1984]. As shown in the laboratory experiment and field observations, the acute angle between the foliation plane and the shear plane decreases with shear strain [Rey *et al.*, 1994; Berthe, 1979; Ramsay, 1980; Lister and Snoke, 1984].

[16] The transition from the brittle to ductile regime may be gradual [Scholz, 2002], so are the evolution of the shear

zone structure [Scholz, 2002; Fagereng and Sibson, 2010] and slip behaviour [Shimamoto, 1989; Kawamoto and Shimamoto, 1998]. Composite slip behaviours are likely in the deep locked zone and the transition zone. The reduced seismic velocity, high Vp/Vs ratio, high seismic reflectivity and strong anisotropy associated with large shear strain in the subduction channel shear zone is probably a manifestation of volumetric increase in clay minerals such as talc [Rey *et al.*, 1994], which can dictate transition in pore-fluid pressure as well as slip behaviour because of its low permeability and weak rheology [Collettini *et al.*, 2009; Niemeijer *et al.*, 2010; Fagereng *et al.*, 2010]. These conditions may also apply for SSEs in other subduction zones as well as deep continental fault zones.

[17] **Acknowledgments.** We thank the entire MASE team for making the data available, A. Frederiksen and M. Bostock for providing the code for our modelling work, and T. Chen for providing slab contour lines for Mexico subduction zone. T.-R. A. Song and Y. Kim are supported by IFREE, JAMSTEC and Tectonics Observatory at Caltech, respectively. Finally, we thank the Editor Michael Wyssession, Pascal Audet, and an anonymous reviewer for helpful comments, which improved the paper.

[18] The Editor thanks Pascal Audet and an anonymous reviewer for assisting in the evaluation of this paper.

References

- Beroza, G., and S. Ide (2011), Slow earthquakes and non-volcanic tremors, *Annu. Rev. Earth Planet. Sci.*, **39**, 271–296, doi:10.1146/annurev-earth-040809-152531.
- Berthe, D. (1979), Orthogenesis, mylonite and non coaxial deformation of granites: The example of the South American shear zone, *J. Struct. Geol.*, **1**, 31–42, doi:10.1016/0191-8141(79)90019-1.
- Bezacier, L., R. Reynard, J. D. Bass, J. Wang, and D. Mainprice (2010), Elasticity of glaucophane, seismic velocities and anisotropy of the subducted oceanic crust, *Tectonophysics*, **494**, 201–210, doi:10.1016/j.tecto.2010.09.011.
- Cassidy, J. F. (1992), Numerical experiments in broadband receiver function analysis, *Bull. Seismol. Soc. Am.*, **82**, 1453–1474.
- Collettini, C., A. Niemeijer, C. Viti, and C. Marone (2009), Fault zone fabric and fault weakness, *Nature*, **462**, 907–910, doi:10.1038/nature08585.
- Crampin, S. (1999), Calculable fluid-rock interactions, *J. Geol. Soc.*, **156**, 501–514, doi:10.1144/gsjgs.156.3.0501.
- Currie, C. A., R. D. Hyndman, K. Wang, and V. Kostoglodov (2002), Thermal models of the Mexico subduction zone: Implications for the megathrust seismogenic zone, *J. Geophys. Res.*, **107**(B12), 2370, doi:10.1029/2001JB000886.
- Fagereng, A., and R. H. Sibson (2010), Melange rheology and seismic style, *Geology*, **38**, 751–754, doi:10.1130/G30868.1.
- Fagereng, A., F. Remitti, and R. H. Sibson (2010), Shear veins observed within anisotropic fabric at high angles to the maximum compressive stress, *Nat. Geosci.*, **3**, 482–485, doi:10.1038/ngeo898.
- Frederiksen, A. W., and M. G. Bostock (2000), Modeling teleseismic waves in dipping anisotropic structures, *Geophys. J. Int.*, **141**, 401–412, doi:10.1046/j.1365-246x.2000.00090.x.
- Fujimoto, Y., Y. Kono, T. Hirajima, K. Kanagawa, M. Ishikawa, and M. Arima (2010), P-wave velocity and anisotropy of lawsonite and epidote blueschist: Constraints on water transportation along subduction oceanic crust, *Phys. Earth Planet. Inter.*, **183**, 219–228, doi:10.1016/j.pepi.2010.09.003.
- Godfrey, N. J., N. I. Christensen, and D. A. Okaya (2000), Anisotropy of schists: Contribution of crustal anisotropy to active source seismic experiments and shear wave splitting observations, *J. Geophys. Res.*, **105**, 27,991–28,007, doi:10.1029/2000JB900286.
- Hacker, B., G. Abers, and S. Peacock (2003), Subduction factory: 1. Theoretical mineralogy, densities, seismic speeds, and H₂O contents, *J. Geophys. Res.*, **108**(B1), 2029, doi:10.1029/2001JB001127.
- Jödicke, H., A. Jording, L. Ferrari, J. Arzate, K. Mezger, and L. Rupke (2006), Fluid release from the subducted Cocos plate and partial melting of the crust deduced from magnetotelluric studies in southern Mexico: Implications for the generation of volcanism and subduction dynamics, *J. Geophys. Res.*, **111**, B08102, doi:10.1029/2005JB003739.
- Kawamoto, E., and T. Shimamoto (1998), The strength profile for biminerale shear zones: An insight from high-temperature shearing experiments on calcite-halite mixtures, *Tectonophysics*, **295**, 1–14, doi:10.1016/S0040-1951(98)00112-7.

- Kern, H., T. I. Ivankina, A. N. Nikitin, T. Lokajicek, and Z. Pros (2008), The effect of oriented microcracks and crystallographic and shape preferred orientation on bulk elastic anisotropy of a foliated biotite gneiss from Outokumpu, *Tectonophysics*, 457, 143–149, doi:10.1016/j.tecto.2008.06.015.
- Kim, Y., R. W. Clayton, and J. M. Jackson (2010), Geometry and seismic properties of the subducting Cocos plate in central Mexico, *J. Geophys. Res.*, 115, B06310, doi:10.1029/2009JB006942.
- Kostoglodov, V., A. Husker, N. M. Shapiro, J. S. Payero, M. Campillo, N. Cotte, and R. W. Clayton (2010), The 2006 slow slip event and nonvolcanic tremor in the Mexican subduction zone, *Geophys. Res. Lett.*, 37, L24301, doi:10.1029/2010GL045424.
- Ligorria, J. P., and C. J. Ammon (1999), Iterative deconvolution and receiver function estimation, *Bull. Seismol. Soc. Am.*, 89, 19–36.
- Lister, G. S., and A. W. Snoke (1984), S-C mylonites, *J. Struct. Geol.*, 6, 617–638, doi:10.1016/0191-8141(84)90001-4.
- Liu, Y., and J. Rice (2009), Slow slip predictions based on granite and gabbro friction data compared to GPS measurements in northern Cascadia, *J. Geophys. Res.*, 114, B09407, doi:10.1029/2008JB006142.
- Mainprice, D., Y. Le Page, J. Rodgers, and P. Jouanna (2008), Ab initio elastic properties of talc from 0 to 12 GPa: Interpretation of seismic velocities at mantle pressures and prediction of auxetic behaviour at low pressure, *Earth Planet. Sci. Lett.*, 274, 327–338, doi:10.1016/j.epsl.2008.07.047.
- Niemeijer, A., C. Marone, and D. Elsworth (2010), Fabric induced weakness of tectonic faults, *Geophys. Res. Lett.*, 37, L03304, doi:10.1029/2009GL041689.
- Obara, K. (2009), Inhomogeneous distribution of deep slow earthquake activity along the strike of the subducting Philippine Sea Plate, *Gondwana Res.*, 16, 512–526, doi:10.1016/j.gr.2009.04.011.
- Pacheco, J. F., and S. K. Singh (2010), Seismicity and state of stress in Guerrero segment of the Mexican subduction zone, *J. Geophys. Res.*, 115, B01303, doi:10.1029/2009JB006453.
- Perez-Campos, X., Y. Kim, A. Husker, P. M. Davis, R. W. Clayton, A. Iglesias, J. F. Pacheco, S. K. Singh, V. C. Manea, and M. Gurnis (2008), Horizontal subduction and truncation of the Cocos Plate beneath central Mexico, *Geophys. Res. Lett.*, 35, L18303, doi:10.1029/2008GL035127.
- Radiguet, M., F. Cotton, M. Vergnolle, M. Campillo, B. Valette, V. Kostoglodov, and N. Cotte (2011), Spatial and temporal evolution of a long term slow slip event: The 2006 Guerrero slow slip event, *Geophys. J. Int.*, 184, 816–828, doi:10.1111/j.1365-246X.2010.04866.x.
- Ramsay, J. G. (1980), Shear zone geometry: A review, *J. Struct. Geol.*, 2, 83–99, doi:10.1016/0191-8141(80)90038-3.
- Rey, P. F., D. M. Fountain, and W. P. Climent (1994), P wave velocity across a noncoaxial ductile shear zone and its associated strain gradient: Consequences for upper crustal reflectivity, *J. Geophys. Res.*, 99, 4533–4548, doi:10.1029/93JB03105.
- Scholz, C. (2002), *The Mechanics of Earthquakes and Faulting*, 471 pp., Cambridge Univ. Press, Cambridge, U. K.
- Schulte-Pelkum, V., G. Monsalve, A. Sheehan, M. R. Pandey, S. Sapkota, R. Bilham, and F. Wu (2005), Imaging the Indian subcontinent beneath the Himalaya, *Nature*, 435, 1222–1225, doi:10.1038/nature03678.
- Shimamoto, T. (1989), The origin of S-C mylonites and a new fault-zone model, *J. Struct. Geol.*, 11, 51–64, doi:10.1016/0191-8141(89)90035-7.
- Song, T.-R. A., and Y. Kim (2012), Anisotropic uppermost mantle in young subducted slab underplating central Mexico, *Nat. Geosci.*, 5, 55–59, doi:10.1038/ngeo1342.
- Song, T.-R. A., D. V. Helmberger, M. R. Brudzinski, R. W. Clayton, P. Davis, X. Perez-Campos, and S. K. Singh (2009), Subducting slab ultra-slow velocity layer coincident with silent earthquakes in southern Mexico, *Science*, 324, 502–506, doi:10.1126/science.1167595.
- Vergnolle, M., A. Walpersdorf, V. Kostoglodov, P. Tregoning, J. A. Santiago, N. Cotte, and S. I. Franco (2010), Slow slip events in Mexico revised from the processing of 11 years GPS observations, *J. Geophys. Res.*, 115, B08403, doi:10.1029/2009JB006852.

Y. Kim, Lamont-Doherty Earth Observatory, Earth Institute at Columbia University, 61 Rte. 9W, Palisades, NY 10964, USA.

T.-R. A. Song, Interior for Research on Earth Evolution, Japan Agency for Marine-Earth Science and Technology Center, 3173-25 Showa-machi, Kanazawa-ku, Yokohama, Kanagawa 237-0005, Japan. (tehrusong@gmail.com)